The Astrophysical Journal, 998:235 (10pp), 2026 February 20 https://doi.org/10.3847/1538-4357/ae328f

Spectral Connection between Far UV and Soft X-Ray Emission from Active Galactic Nuclei Using AstroSat

Shrabani Kumar[1], G. C. Dewangan[1], K. P. Singh[2,3], P. Gandhi[4], L. Mallick[5,6,9], G. C. Stewart[7], S. Bhattacharyya[3], and S. Chandra[8]
[1] Inter-University Centre for Astronomy and Astrophysics, Pune 411007, India; kmrshrab@gmail.com
[2] Indian Institute of Science Education and Research Mohali, Knowledge City, Sector 81, Manauli P.O., SAS Nagar, 140306, Punjab, India
[3] Department of Astronomy and Astrophysics, Tata Institute of Fundamental Research, 1 Homi Bhabha Road, Mumbai 400005, India
[4] School of Physics & Astronomy, University of Southampton, Highfield SO17 1BJ, UK
[5] Department of Physics & Astronomy, University of Manitoba, Winnipeg, Manitoba R3T 2N2, Canada
[6] Canadian Institute for Theoretical Astrophysics, University of Toronto, 60 St. George Street, Toronto, Ontario M5S 3H8, Canada
[7] Department of Physics and Astronomy, The University of Leicester, University Road, Leicester LE1 7RH, UK
[8] Center for Space Research, North-West University, Potchefstroom 2520, South Africa
Received 2024 October 19; revised 2025 December 23; accepted 2025 December 31; published 2026 February 12

Abstract

We present the UV/X-ray joint spectral analyses of four Seyfert 1 galaxies (PG 0804+761, NGC 7469, SWIFT J1921.1-5842, and SWIFT J1835.0+3240) using the data acquired with the Ultraviolet Imaging Telescope and Soft X-ray Telescope on board AstroSat. We model the intrinsic UV/X-ray continuum with the accretion disk and warm and hot Comptonization using the `OPTXAGNF` and `FAGNSED` models, where the disk seed photons are Comptonized in the warm and hot corona. The Eddington ratio of the four Seyferts ranges from 0.01 to 1. In the case of SWIFT J1835.0+3240, we infer a compact warm corona ($R_{\rm warm} - R_{\rm hot} \lesssim 18r_g$), while PG 0804+761, NGC 7469, and SWIFT J1921.1-5842 may exhibit a larger warm Comptonizing region ($\gtrsim 32r_g$). We could constrain the spin parameter in PG 0804+761, $a^\star = 0.76^{+0.08}_{-0.20}$ (1σ error), with the `FAGNSED` model. In SWIFT J1835.0+3240 and SWIFT J1921.1-5842, the UV/X-ray spectral variability may be driven by the thermal Comptonization of the disk seed photons in the hot corona. Furthermore, the observed spectral hardening with the decrease in disk temperature and accretion rate compared to earlier observations may indicate a state transition in SWIFT J1835.0+3240 from a high/soft to a low/hard state.

Unified Astronomy Thesaurus concepts: Accretion (14); Seyfert galaxies (1447); Ultraviolet spectroscopy (2284)

1. Introduction

The primary emission from radio-quiet active galactic nuclei (AGN) consists of the Big Blue Bump (BBB), the soft X-ray excess component, and the broadband X-ray power-law emission. The BBB emission generally peaks in the extreme UV band and spans over near-infrared to extreme UV bands (A. Koratkar & O. Blaes 1999). This component is generally contaminated with broad/narrow emission lines, narrow absorption lines, and emission from the host galaxy and can be reddened due to the host galaxy. The BBB component is thought to be the direct consequence of the accretion flow arising from the accretion disk around central supermassive black holes in AGN (N. I. Shakura & R. A. Sunyaev 1973). However, the observed UV continua are generally found to be redder than the theoretical accretion disk spectrum. Using far-UV spectra of eight bright Seyfert 1 galaxies acquired with AstroSat observations, we showed that the observed spectra are generally consistent with standard disk models, but the disks appear truncated (S. Kumar et al. 2023, hereafter Paper I). It is unclear if the apparent truncation of disks is real or just due to the deficit of UV emission from the innermost accretion disks. In this aspect, it is important to understand the connection of disk emission with the soft X-ray emission.

The X-ray spectra of many Seyfert 1 galaxies show the presence of soft excess components. First observed by K. Singh et al. (1985) in the HEAO-1 data and K. A. Arnaud et al. (1985) in the EXOSAT data, the soft excess is identified as an excess over the broadband X-ray power-law continuum in the soft X-ray band below 2 keV. The temperature of this blackbody-like component is found to be remarkably similar, around ∼0.1 keV across AGN with different black hole masses (M. Gierliński & C. Done 2004; L. Mallick et al. 2022). In some AGN, the short timescale variability of the soft X-ray excess emission suggests that this component arises from the innermost regions. The exact nature and origin of the soft excess still remain uncertain. Though several models have been proposed to explain this emission component, currently, two competing models, warm Comptonization and blurred reflection, can both explain the origin of the soft excess. X-ray reflection from a partially ionized accretion disk can give rise to many emission lines and a Thomson scattered continuum. The relativistic blurring due to special and general relativistic effects on the numerous emission lines and the scattering continuum can give rise to a smooth continuum component that mimics the soft excess component (I. George & A. Fabian 1991; J. García et al. 2014). However, the blurred reflection spectra inferred from the broad iron line when extrapolated to the soft X-ray band below 2 keV appears to be insufficient for the observed strong soft excess in some AGN (e.g., Ark 120; L. Mallick et al. 2017). This problem can be alleviated by high-density reflection models (e.g., J. A. García et al. 2016; L. Mallick et al. 2018). Another popular model for

[9] CITA National Fellow.

the soft excess is the warm Comptonization model. In this case, the soft excess component is treated as a different continuum component. This is believed to originate from a warm plasma ($kT_w \sim 0.1$–1 keV) with large optical depth ($\tau \sim 10$–40) in the inner region of a truncated accretion disk (P. O. Petrucci et al. 2018). The outer area of the accretion disk may still behave as a standard accretion disk. These warm layers of plasma Compton upscatter the disk seed photons, giving rise to the apparent soft excess (C. Done et al. 2012; A. Kubota & C. Done 2018). The only difficulty in this model is fine-tuning the heating and cooling of the warm corona to obtain the fixed temperature observed for a wide range of black hole masses.

These two models, blurred reflection and warm Comptonization, often produce statistically equivalent results, making it difficult for them to be distinguished (G. C. Dewangan et al. 2007; M. Pal et al. 2016; S. Waddell et al. 2019; S.-J. Chen et al. 2025). R. Middei et al. (2020) studied the narrow line Seyfert 1 Mrk 359 using XMM-Newton–NuStar observations. They tested both the relativistic blurred reflection and warm Comptonization model and found that the latter reproduced the soft excess better. Similarly, for Zw 229.015, S. Tripathi et al. (2019) observed the warm Comptonization to describe the soft excess better than other models. H. Noda et al. (2011) found the soft X-ray variability does not follow the fast variability observed in the hard X-ray for Mrk 509. If X-ray reflection is the origin (or partial origin) for soft X-ray excess, then a correlation between the soft and hard X-ray variability is expected (R. Boissay et al. 2014; L. Mallick et al. 2018). In the warm Comptonization model, since the warm corona is either the innermost part of the accretion disk or the warm layer on it, such warm coronae can modify the accretion disk substantially. Hence, it is important to study the connection between the accretion disk UV emission and soft excess emission.

In this paper, we extend our work presented in Paper I on far-UV spectroscopy of AGN and include soft X-ray data acquired simultaneously with AstroSat. We perform joint spectral analysis of far-UV and the soft X-ray data on four AGN and study the spectral connection between the accretion disk and the soft X-ray excess. The broadband spectral energy distribution (SED) of PG0804 is presented for the first time here. This paper is organized as follows. We describe the observations and data reduction in Section 2 and perform joint spectral analysis in Section 3. We discuss our results in Section 4, followed by a summary in Section 5.

2. Observations and Data Reduction

We utilized the simultaneously acquired UV and X-ray spectral data from AstroSat (K. P. Singh et al. 2014) of four type 1 AGN: PG 0804+761 (hereafter PG0804), NGC 7469, SWIFT J1921.1-5842 (hereafter SWIFT1921), and SWIFT J1835.0+3240 (hereafter SWIFT1835). AstroSat is India's first space observatory that covers UV to X-rays with its suit of four coaligned payloads: the Ultraviolet Imaging Telescope (UVIT; S. Tandon et al. 2017, 2020), the Soft X-ray Telescope (SXT; K. P. Singh et al. 2016; K. Singh et al. 2017), the Large Area X-ray Proportional Counters (L. Yadav et al. 2016; H. Antia et al. 2017), and the Cadmium-Zinc-Telluride Imager (S. V. Vadawale et al. 2016). In this paper, we used the far-UV and X-ray data simultaneously acquired with the UVIT and SXT, respectively.

2.1. Ultraviolet Imaging Telescope

The UVIT consists of two telescopes: one observes in the far-ultraviolet band (1200–1800 Å), referred to as the FUV channel. The other telescope observes in the near-ultraviolet band (2000–3000 Å) and the visible band (3200–5500 Å), referred to as the NUV and VIS channels, respectively. The visible band is used to correct telescope drift while observing any source. Both the FUV and NUV channels have several broadband filters. In addition, the FUV channel contains two slitless low-resolution gratings (hereafter, FUV-G1 and FUV-G2) that are orthogonally oriented to each other. The NUV channel has only one slitless grating (hereafter, NUV-G). The spatial resolution of FUV and NUV broadband filter is 1″–1.″5. The FWHM for the FUV gratings in the −2 order is ∼14.3 Å and that for the NUV grating in the −1 order is ∼33 Å.

We described the UVIT data reduction in detail in Paper I. Here, we briefly mention the steps. We obtained the level 1 data from the AstroSat data archive[10] and processed them using the CCDLAB pipeline software (J. E. Postma & D. Leahy 2017). We extracted the source spectra from the −2 order of the FUV grating and −1 order of the NUV grating and the corresponding background spectra from a source-free region following the method described in G. C. Dewangan (2021) and the tools available in the UVITTools.jl package.[11] We also used the response files made available as part of the UVITTools.jl package.

2.2. Soft X-Ray Telescope

The SXT is a focusing X-ray telescope that uses conical mirrors to focus the X-ray photons onto a CCD detector (K. Singh et al. 2017). It observes in the photon counting mode and is sensitive to the 0.3–7 keV energy band. The field of view is ∼40′, and the energy resolution is ∼150 eV at 6 keV.

We processed the level 1 data using the SXT pipeline software AS1SXTLevel2-1.4b available at the SXT payload operation center (POC).[12] This generates the clean event file for each orbit. We merged the clean event files using the SXT merger tool SXTMerger.[13] We extracted the source spectra from the final clean image file using the tool XSELECT available in the HEASoft package (version 6.29). We used the background spectrum (SkyBkg_comb_EL3p5_Cl_Rd16p0_v01.pha), instrument response (redistribution matrix file: sxt_pc_mat_g0to12.rmf), and effective area (auxiliary response file : sxt_pc_excl00v04_20190608.arf) from the SXT POC website. We grouped each PHA (pulse height amplitude) spectral data set with a minimum 25 counts bin^{-1} using the ftool FTGROUPPHA available within HEASoft.

3. UV–X-Ray Joint Spectral Analysis

In Paper I, we analyzed the UVIT grating spectra of the AGN listed in Table 1. We accounted for the intrinsic and Galactic extinctions, host galaxy contribution, broad line or narroow line region (BLR/NLR) emission, and Fe II emission and obtained the intrinsic UV continuum emission. We fitted the continuum with a simple multitemperature disk blackbody model `DISKBB`, which allowed us to estimate the peak inner disk temperatures.

[10] https://astrobrowse.issdc.gov.in/astro_archive/archive/Home.jsp
[11] https://github.com/gulabd/UVITTools.jl
[12] https://www.tifr.res.in/~astrosat_sxt/sxtpipeline.html
[13] https://github.com/gulabd/SXTMerger.jl

Table 1
List of AstroSat/UVIT and SXT Observations

Source Name	Observation ID	Instrument	Date of Observation	Exposure Time (ks)	Count Rate (counts s^{-1})
PG0804	G07_062T01_9000001560	AstroSat/UVIT/FUV-G2	2017-09-25	4.1	8.9 ± 0.05
	G07_062T01_9000001560	AstroSat/UVIT/NUV-G	2017-09-25	4.0	59 ± 0.1
	G07_062T01_9000001560	AstroSat/SXT	2017-09-(25–26)	14.2	0.208 ± 0.004
NGC7469	G08_071T02_9000001620	AstroSat/UVIT/FUV-G1	2017-10-18	3.4	5.73 ± 0.04
		AstroSat/UVIT/FUV-G2	2017-10-18	4.0	7.88 ± 0.05
	G08_071T02_9000001620	AstroSat/SXT	2017-10-(15–19)	108	0.599 ± 0.003
SWIFT1921	A04_218T08_9000002236	AstroSat/UVIT/FUV-G1	2018-07-17	5.7	8.50 ± 0.04
		AstroSat/UVIT/FUV-G2	2018-07-18	5.4	9.72 ± 0.04
	A04_218T08_9000002236	AstroSat/SXT	2018-07-(17–19)	29	0.653 ± 0.005
SWIFT1835	A04_218T04_9000002086	AstroSat/UVIT/FUV-G1	2018-05-10	3.2	1.04 ± 0.02
	A04_218T04_9000002086	AstroSat/SXT	2018-05-(9–10)	20	0.338 ± 0.004

Note. The last column is the background-corrected net count rate of the sources in the −2 order of FUV gratings or −1 order of NUV grating.

Then, we replaced DISKBB with OPTXAGNF (disk component only) to infer the inner disk geometry.

In this paper, we use the best-fit model with the continuum component as OPTXAGNF and construct the broadband SED by fitting the SXT and UVIT spectral data jointly.

We initially analyze the X-ray spectrum for each AGN to investigate the presence of different spectral components, such as the soft X-ray excess, warm, or neutral absorbers. Next, we model the UVIT/SXT spectra jointly. In this case, we fix the parameters associated with the emission and absorption lines, as well as warm and neutral absorbers, to those obtained during separate UV and X-ray spectral fittings. We use OPTXAGNF (C. Done et al. 2012) or FAGNSED[14] (A. Kubota & C. Done 2018; S. Hagen & C. Done 2023) models to represent the underlying UV/X-ray continuum. FAGNSED model is an upgraded version of the OPTXAGNF model. In OPTXAGNF, the standard accretion disk is truncated at a radius r_{cor}, below which the disk seed photons are Comptonized in warm ($kT_w \sim 0.1$–1 keV) and hot ($kT = 100$ keV) coronae to produce the soft X-ray excess and the X-ray power-law components, respectively. The disk emission beyond the r_{cor} emits as a modified blackbody emission. However, unlike OPTXAGNF, the Comptonization region is radially stratified into warm and hot coronae in FAGNSED. The warm Comptonizing corona exists between R_{warm} and R_{hot} over a passive disk, and the inner hot flow extends from R_{hot} to R_{ISCO}. The sum total of Comptonized disk photons in each radial bin produces the overall soft excess emission. Therefore, FAGNSED provides the radial extent of each emitting region and improves our understanding of the accretion disk better than the OPTXAGNF model. The free parameters of the OPTXAGNF model are the logarithm of the Eddington ratio ($\log(L/L_{Edd})$), black hole spin ($a^\star$), coronal radius (r_{cor}), warm corona temperature (kT_w), optical depth of the warm corona (τ_w), X-ray photon index (Γ), and the fraction of power-law emission below r_{cor} (f_{pl}). The relevant parameters of FAGNSED are the logarithm of the Eddington ratio, spin parameter ($a^\star$), the inclination angle, the temperature of the warm corona (kT_w), photon index of the X-ray power law (Γ_{hot}) and soft X-ray excess (Γ_{warm}), outer radius of the hot corona (R_{hot}) and the radius of warm corona (R_{warm}), and the maximum height of the X-ray corona. We fixed the normalization to 1 for both these models and varied the rest of the parameters during the joint UV–X-ray spectral fitting unless mentioned otherwise. The errors are quoted at a 90% confidence interval unless mentioned otherwise.

[14] https://github.com/scotthgn/fAGNSED

3.1. PG 0804+761

We fitted the 2–7 keV SXT spectral data with the Galactic absorbed power-law model. Extending the data and model to 0.7 keV, we observed some soft X-ray excess emission (see Figure 1). We added a ZBBODY model in the 0.7–7 keV band to account for this excess emission. This did not improve the fit significantly ($\Delta\chi^2 = 2$), possibly due to the low signal-to-noise of the SXT data. With only the Galactic absorbed power law in the 0.7–7 keV band, the final best-fit χ^2 per degree of freedom (dof) =60/52.

Next, we included previously fitted (with OPTXAGNF) FUV-G1 and NUV-G spectra in the SXT spectral data. We removed the ZPOWERLAW and the ZBBODY, which are accounted for by the OPTXAGNF model component. The model expression for the joint UV/X-ray spectral fitting in XSPEC is CONSTANT × TBABS × REDDEN × GABS × [PLABS(OPTXAGNF) + GAUSSIAN_{UV}]. Since the soft excess is weak in the SXT spectrum, we fixed the kT_w at 0.26 keV and the τ at 8 following P. O. Petrucci et al. (2018). We obtained a lower limit in the $f_{pl} > 0.3$. We obtained the final best-fit $\chi^2/\text{dof} = 454/391$ with OPTXAGNF (see Table 2). The unabsorbed data, SED, and absorbed SED are shown in Figure 2(a).

We also modeled the UV/X-ray spectral data with the FAGNSED model. We replaced only the OPTXAGNF model component with the FAGNSED. The inclination angle is fixed at 30°, as we obtained an upper limit of 60°. We found the $\chi^2/\text{dof} = 436.4/390$ with the FAGNSED model. We found the spin parameter, $a^\star = 0.76^{+0.08}_{-0.20}$ (1σ error), and the $R_{hot} = 5.4^{+1.9}_{-0.9}\, r_g$ (1σ error). The remaining best-fit parameters of FAGNSED are listed in Table 3. In Figure 2(b), we show the unabsorbed and absorbed SED and the model components.

3.2. NGC 7469

We modeled the X-ray spectrum in the 2–7 keV range with a Galactic absorbed power law and a narrow ($\sigma = 10$ eV) Fe Kα emission line at ∼6.5 keV. The soft X-ray excess emission is apparent above the power law ($\Gamma \sim 1.67$; Figure 1) at low

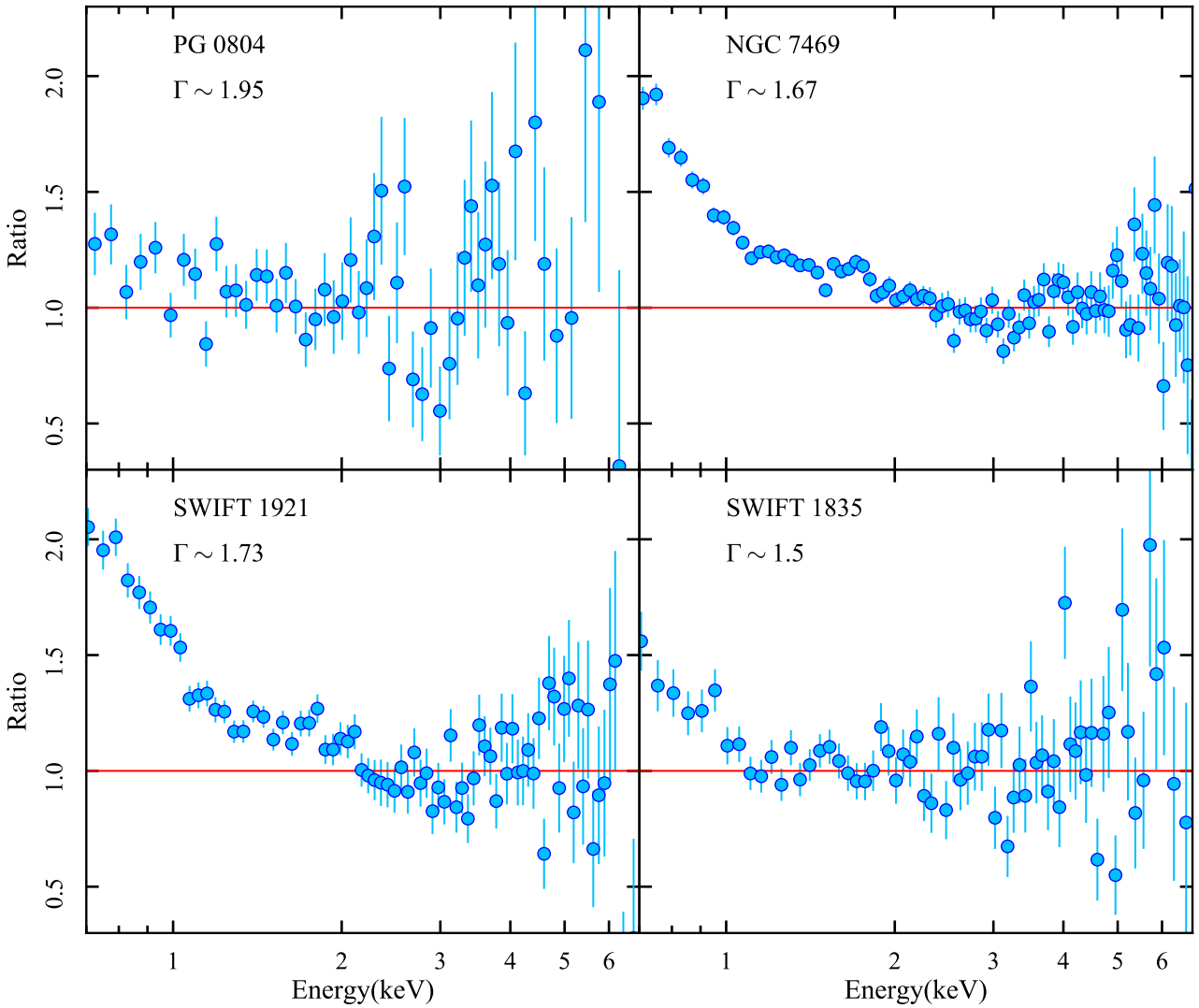

Figure 1. Soft X-ray excess observed in the four objects shown by the plotting ratio (data/model). The power law (modified by Galactic absorption) is fitted between the 2–10 keV band and then extrapolated to 0.7 keV. The respective Γ is 1.95 (PG0804), 1.67 (NGC 7469), 1.73 (SWIFT1921), and 1.5 (SWIFT1835).

Table 2
Best-fit Parameters of the OPTXAGNF and Emission Line Components Fitted to the UV/X-Ray Spectra.

Model	Parameter	PG0804	NGC 7469	SWIFT1921	SWIFT1835
OPTXAGNF	$\log(L/L_{\rm Edd})$	$-0.270^{+0.003}_{-0.003}$	$-0.18^{+0.20}_{-0.09}$	$-0.34^{+0.06}_{-0.04}$	$-1.8^{+0.1}_{-0.1}$
	$a^{\star}$	0.998 (f)	$0.37^{+0.29}_{-0.30}$	0.998 (f)	0.998 (f)
	$r_{\rm cor}$	$1.6^{+0.1}_{-0.1}$	39^{+20}_{-19}	$95.3^{+11.7}_{-10.2}$	$16.3^{+12.2}_{-5.8}$
	kT_w	0.26 (f)	$0.31^{+0.05}_{-0.04}$	$0.12^{+0.02}_{-0.02}$	$0.12^{+0.06}_{-0.04}$
	τ	8 (f)	$13.3^{+2.1}_{-3.1}$	$26.5^{+5.6}_{-3.9}$	>20
	Γ	$2.0^{+0.1}_{-0.1}$	$1.78^{+0.16}_{-0.17}$	$2.04^{+0.05}_{-0.05}$	$1.52^{+0.07}_{-0.07}$
	$f_{\rm pl}$	>0.3	$0.17^{+0.23}_{-0.07}$	$0.35^{+0.03}_{-0.04}$	$0.8^{+0.2}_{-0.2}$
XABS	$N_{\rm H}(10^{22}\ {\rm cm}^{-2})$	⋯	$3.3^{+0.3}_{-0.6}$	36 (f)	⋯
	$\log\xi$	⋯	<−1.6	0.2 (f)	⋯
	$f_c^{\rm xabs}$	⋯	$0.87^{+0.04}_{-0.07}$	0.47 (f)	⋯
Fe Kα	norm (10^{-4})	⋯	$0.7^{+0.4}_{-0.4}$	⋯	⋯
χ^2/dof		454/391	395.9/361	362.9/324	262.0/238

Note. (f): Parameter frozen.

energies (∼2 keV). Adding a ZBBODY component to account for the soft excess emission improved the χ^2 by 94 (in 0.7–7 keV band) for two additional free parameters, blackbody temperature (kT), and the normalization. The XMM-Newton-RGS (Reflection Grating Spectrometer) and Chandra-HETGS spectra of NGC 7469 showed the presence of multilayer warm absorber components with column density and the ionization varying in the range $N_{\rm H}$ ∼ 0.7–5.2 × 10^{21} and

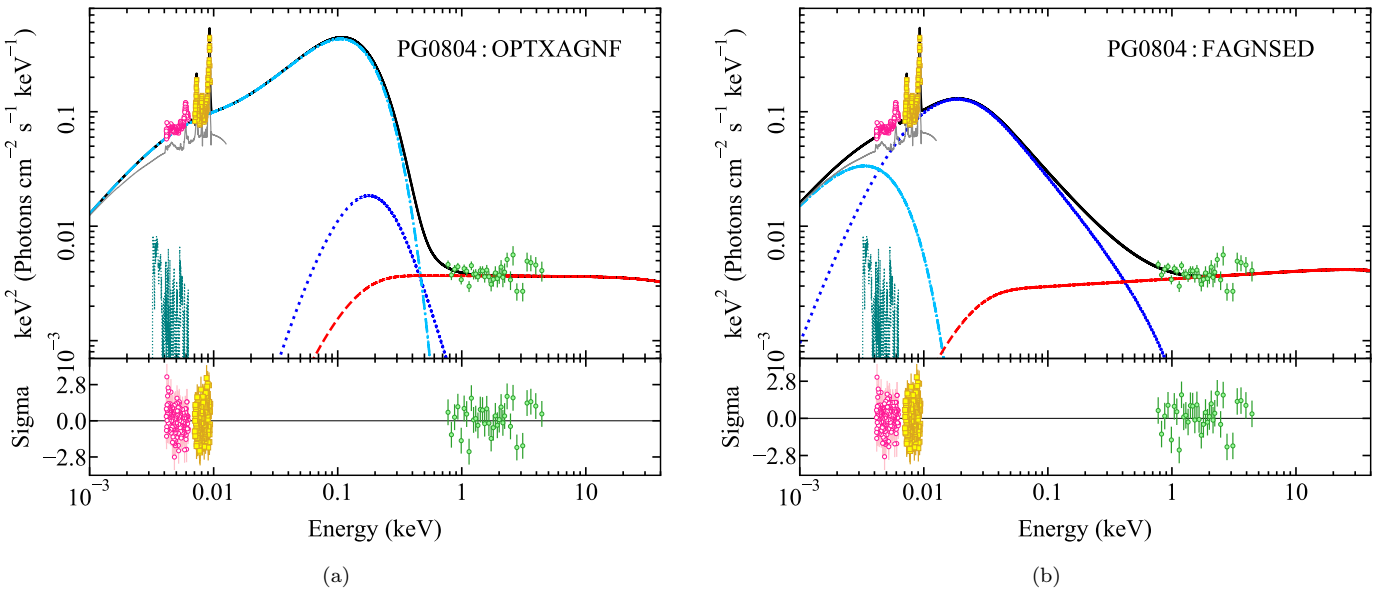

Figure 2. Results of UV/X-ray broadband spectral analysis. Upper panels: the best-fit total unabsorbed model (black), absorbed model (gray), and the absorption-corrected spectral data set UVIT/FUV grating (yellow), UVIT/NUV grating (pink), and the SXT (green). Also shown are the different model components: accretion disk (cyan), soft excess (blue), X-ray power law (red), and the Fe II complex (teal). Lower panels: the fit residuals in terms of data − model/error.

Table 3
Best-fit Parameters of FAGNSED Model Fitted to AstroSat Spectral Data

FAGNSED	$\log \frac{\dot{M}}{M_{\rm Edd}}$	a [a]	$kT_{\rm warm}$	$\Gamma_{\rm hot}$	$\Gamma_{\rm warm}$	$R_{\rm hot}$	$R_{\rm warm}$	χ^2/dof
PG0804	$-0.86^{+0.05}_{-0.07}$	$0.76^{+0.08}_{-0.20}$ [a]	0.26 (f)	$1.94^{+0.15}_{-0.15}$	$3.3^{+0.3}_{-0.2}$	$5.4^{+1.9}_{-0.9}$ [a]	$55.6^{+48.6}_{-15.2}$	436.4/390
NGC 7469	$-0.39^{+0.08}_{-0.08}$	<0.67	$0.27^{+0.04}_{-0.03}$	$1.89^{+0.16}_{-0.18}$	$2.28^{+0.19}_{-0.13}$	$11.7^{+3.8}_{-5.4}$	252^{+90}_{-106}	391.6/361
SWIFT1921	$-0.19^{+0.21}_{-0.03}$	<0.86	$0.12^{+0.04}_{-0.02}$	$2.03^{+0.05}_{-0.05}$	$2.7^{+1.2}_{-0.2}$	$14.1^{+1.0}_{-7.1}$	330^{+42}_{-274}	364.0/323
SWIFT1835	$-1.8^{+0.1}_{-0.1}$	0.998 (f)	$0.12^{+0.07}_{-0.02}$	$1.52^{+0.05}_{-0.08}$	<2.25	$9.9^{+3.7}_{-1.9}$	$18.9^{+7.2}_{-3.9}$	259.6/238

Notes. The inclination angles are fixed at 30° (PG0804), 20° (NGC 7469), 31° (SWIFT1921), and 30° (SWIFT1835). The maximum height of the corona is fixed at 10 r_g, and the hot corona temperature is fixed at 100 keV.
[a] 68% confidence interval.

$\log \xi \sim 1.9 - 3.3$, respectively (M. Mehdipour et al. 2018; S. Grafton-Waters et al. 2020). Further, they found the total column density considering all the absorbers to be similar over time although the ionization levels of the different components varied slightly. Therefore, we also tested the presence of a warm absorber using the XABS model by varying the $N_{\rm H}$ within the range provided by M. Mehdipour et al. (2018). Since we could not constrain the column density, we fixed the $N_{\rm H}$ to the highest value observed by S. Grafton-Waters et al. (2020), 5×10^{21} cm^{-2}; the turbulent velocity v at 100 km s^{-1}; and the redshift at 0.016 (S. Grafton-Waters et al. 2020). This resulted in a marginal improvement in the statistic, $\Delta\chi^2 = 5$, for one additional free parameter, $\log \xi = 3.21^{+0.49}_{-0.34}$. Further addition of the XABS component did not change the statistics. Therefore, we included only one warm absorber component. The final XSPEC model expression for the SXT spectrum is TBABS × XABS × [ZPOWERLAW + FeKα + ZBBODY]. We obtained the final χ^2/dof = 129.6/84 with a gain shift of 61 eV and a systematic error of 2%.

Next, we included the previously fitted UVIT grating spectra with OPTXAGNF, emission/absorption lines (GAUSSIAN$_{\rm UV}$/GABS), Fe II emission, and starburst emission (SB3) and removed the ZPOWERLAW and ZBBODY. All these components are corrected for Galactic extinction. Again, we used 2% systematic error and a gain shift fixed at that obtained during the SXT spectral analysis. We obtained an unusually flat spectrum ($\Gamma \sim 1.4$). Therefore, we varied the $N_{\rm H}$ in the XABS model, which was fixed at 5×10^{21} cm^{-2}. We also varied the ionization parameter $\log \xi$ and the covering fraction $f_c^{\rm xabs}$. We found the best-fit value for $N_{\rm H} \sim 3.3 \times 10^{22}$ cm^{-2}, with the absorber being neutral. This $N_{\rm H}$ is slightly larger than that obtained previously (M. Mehdipour et al. 2018; U. Peretz et al. 2018; S. Grafton-Waters et al. 2020). This could have resulted due to the poor spectral resolution of SXT. However, we found the best-fit photon index ∼1.78 and the spin parameter ∼0.37 (Table 2). We obtained the final χ^2/dof = 395.9/361 with the model expression REDDEN × TBABS × [SB 3 + XABS × GABS × (OPTXAGNF + GAUSSIAN$_{\rm UV}$ + FeKα)]. The unabsorbed data, SED, and fit residuals are shown in Figure 3(a). With the FAGNSED model as a UV–X-ray continuum component, we found a substantially large emitting region contributing to the soft excess (see Figure 3(b)). We obtained the best-fit χ^2/dof = 391.6/361 with the FAGNSED model (Table 3). We show the unabsorbed data, model, and fit residuals in Figure 3(b).

3.3. SWIFT J1921.1−5842

We fitted the SXT spectrum with a Galactic absorbed power law in the 2–7 keV band. We observed an excess emission

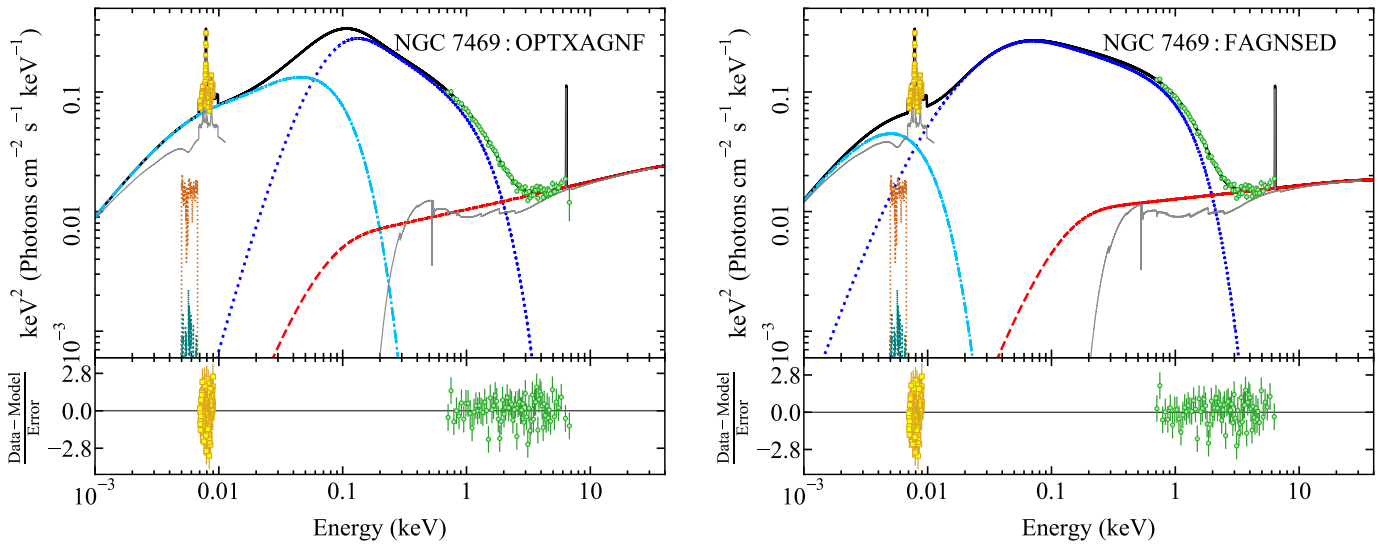

Figure 3. Same as Figure 2 but for NGC 7469. The additional model component, the starburst SB3 template, is shown in orange.

over the power law ($\Gamma \sim 1.7$; see Figure 1) below 2 keV. We used a ZBBODY to account for this excess emission. This improved the χ^2 by 57 (in 0.7–7 keV band) for two additional free parameters. Next, we incorporated the warm absorber model XABS to investigate the presence of this component. This improved the χ^2 by 9 for three additional free parameters, absorption column density ($N_{\rm H}$), covering fraction ($f_c^{\rm xabs}$), and the ionization ($\log \xi$). We obtained an upper limit on the ionization parameter ($\log \xi < 2.1$) of the warm absorber. Therefore, we fixed the ionization parameter $\log \xi$ at 0.2 as obtained by R. Ghosh & S. Laha (2020) in their broadband SED modeling utilizing non-simultaneous XMM-Newton and NuStar observations. We found the warm absorber column density $N_{\rm H} = 3.6^{+0.5}_{-0.1} \times 10^{23}{\rm cm}^{-2}$ and $f_c^{\rm xabs} = 0.5^{+0.5}_{-0.1}$. We obtained the final $\chi^2/{\rm dof} = 84/67$ after using a ~40 eV gain shift to the SXT spectral data using the gain fit command in XSPEC. The final model expression in XSPEC for the SXT spectrum: TBABS × XABS × (ZPOWERLAW + ZBBODY).

Next, we included the UVIT/grating spectra to construct the broadband SED. We used the best-fit model consisting of OPTXAGNF as the continuum component from Paper I. The other model components include emission and absorption lines from the BLR/NLR. We fixed the UV emission and absorption line parameters and the cross-normalization constant between the gratings. Also, we fixed the XABS model parameters to those obtained during the SXT spectral fitting, as varying these parameters during the joint modeling have no effect on the statistic. We could not constrain the spin parameter, which we fixed to 0.998 (R. Ghosh & S. Laha 2020). The final model is REDDEN × TBABS × XABS × (OPTXAGNF + GAUSSIAN$_{\rm UV}$). We obtained $\chi^2/{\rm dof} = 362.9/324$ in the joint UV–X-ray spectral modeling (Table 2). In Figure 4(a), we showed the unabsorbed SED, data, and fit residuals. The FAGNSED model as a broadband continuum component resulted in a similar fit as with the OPTXAGNF model. We listed the best-fit parameters in Table 3. The unabsorbed data, SED and fit residuals are shown in Figure 4(b).

3.4. SWIFT J1835.0+3240

The soft excess emission is shown in Figure 1 over the Galactic absorbed power law in the energy range of 2–7 keV. Adding a ZBBODY improved the χ^2 by 16 (in 0.7–7 keV band) for two additional free parameters and the $\chi^2/{\rm dof} = 79/65$. We also tested for the presence of a warm absorber component by fixing the parameters to the values obtained by F. Ursini et al. (2018). The addition of this component (XABS) significantly worsened the fit. Therefore, we varied the covering fraction of the absorber. This resulted in a covering fraction close to zero. We fixed the covering fraction to 1 and varied the ionization parameter. The χ^2 remained the same as that without the warm absorber model, and we could obtain the lower limit of 3.32 for $\log \xi$. Therefore, we did not include this component for this source. We obtained the final $\chi^2/{\rm dof} = 79/65$ after using a gain shift of 34 eV for the SXT spectral data. The XSPEC model expression is TBABS × (ZPOWERLAW + ZBBODY).

Next, we added the UVIT/grating (FUV-G2) spectrum with the best-fit model components being OPTXAGNF and three emission lines corrected for Galactic reddening. We obtained similar statistics for the spin parameter at 0.998 and 0 although the Eddington ratio and the $r_{\rm cor}$ differ in each case.

We obtained the $L/L_{\rm Edd} \sim 0.02$ and $r_{\rm cor} \sim 51\, r_g$ for $a^\star = 0$ and the $L/L_{\rm Edd} \sim 0.01$ and $r_{\rm cor} \sim 14\, r_g$ for $a^\star = 0.998$. For both spin cases, the photon index Γ ($\sim$ 1.56) and $\chi^2/{\rm dof}$ (=262/238) remained unchanged. The model expression with OPTXAGNF as the continuum component is REDDEN × TBABS × (OPTXAGNF + GAUSSIAN$_{\rm UV}$). In Table 2, we listed the best-fit parameters with the spin parameter fixed at 0.998. The unabsorbed SED, data, and the residuals are shown in Figure 5(a). With FAGNSED as a UV–X-ray continuum component, we found similar best-fit model parameters (see Table 3). We show the unabsorbed data, SED, and residuals in Figure 5(b).

4. Results and Discussion

We analyzed the simultaneous UV–X-ray spectra of four type 1 AGN observed with AstroSat. We used the models

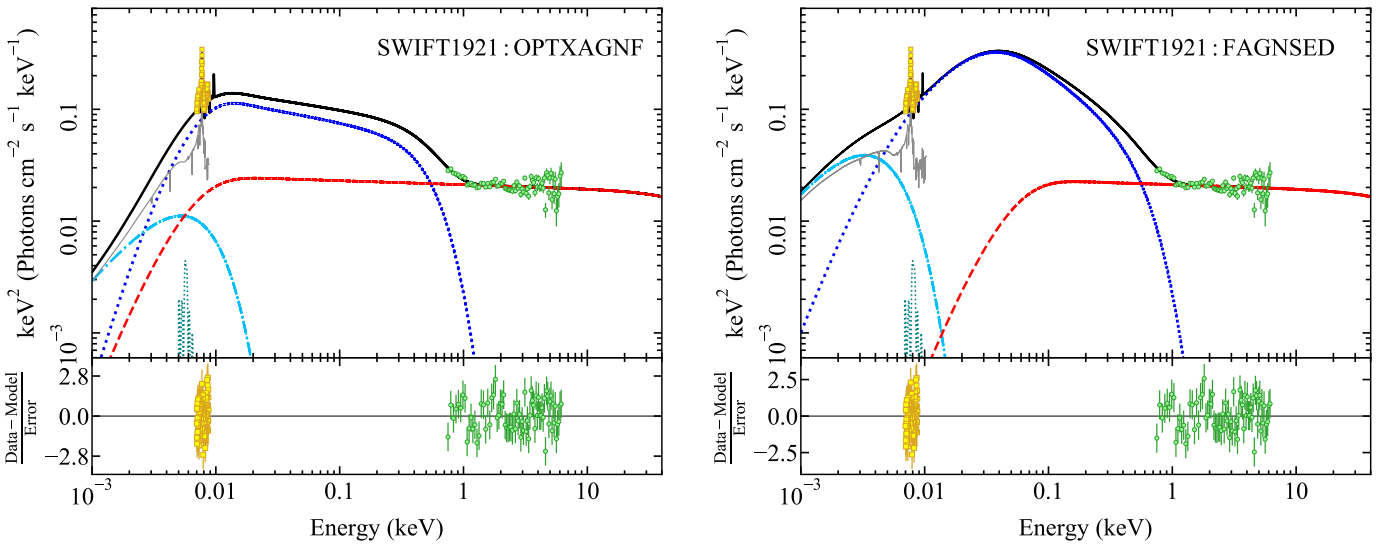

(a) (b)

Figure 4. Same as Figure 2 but for SWIFT1921.

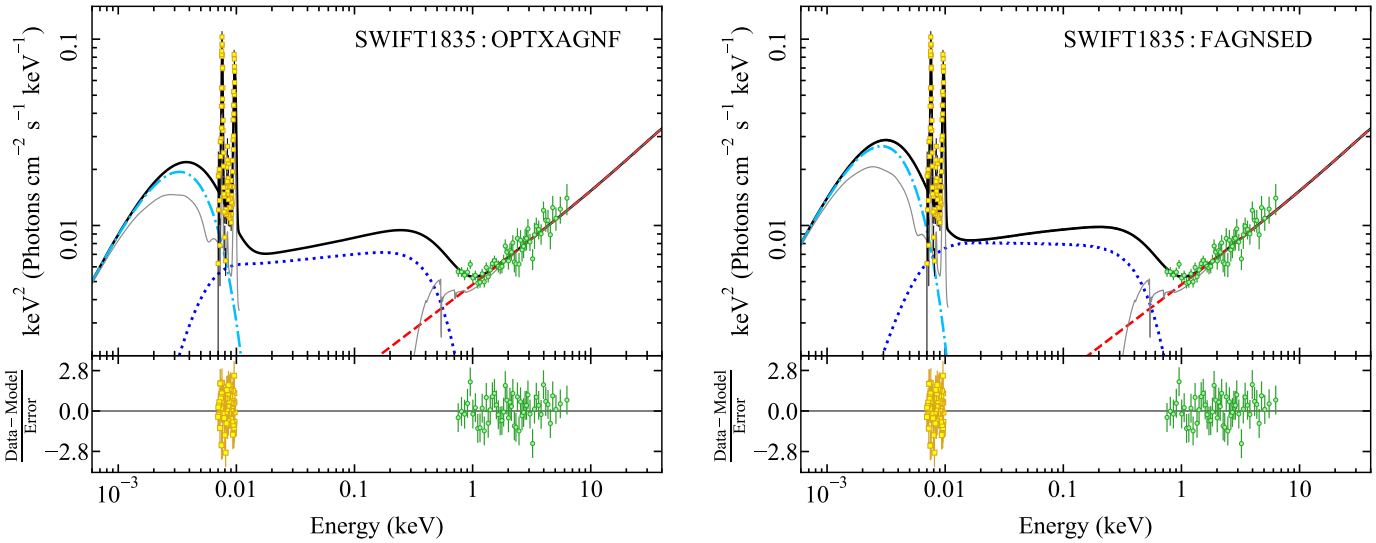

(a) (b)

Figure 5. Same as Figure 2 but for SWIFT1835.

OPTXAGNF and FAGNSED to fit the broadband SEDs for all four sources. The soft X-ray excess emission below 2 keV is well described by warm Comptonization of the disk seed photons. We obtain the X-ray power-law photon index in the range of ∼1.5–2.1. The inner accretion disk appears to be converted into warm Comptonizing plasma in all sources. The disk (0.001–0.01 keV), soft X-ray (0.5–2 keV), and hard X-ray (2–10 keV) fluxes are listed in Table 4.

4.1. PG 0804+761

The accretion flow geometry was better described by the FAGNSED model, an outer standard disk, inner warm corona, and hot corona. In this case, the soft X-ray excess emission in the 0.2–2 keV band is dominated by the thermal Comptonization of disk seed photons, while in OPTXAGNF, a fraction of the soft excess is contributed by color-corrected disk blackbody emission. The difference in the underlying geometry and the assumptions between these two models may be the reason behind this difference. We obtained the Eddington ratio ∼0.2–0.5, similar to that obtained by P. O. Petrucci et al. (2018; Eddington ratio ∼0.4).

4.2. NGC 7469

Based on our UV/X-ray SED, we estimated the bolometric luminosity $\sim 9 \times 10^{44}$ erg s^{-1}, corresponding to an Eddington ratio of 0.7. During the observation performed in 1996 with IUE/XTE (X-ray Timing Explorer), P. O. Petrucci et al. (2004) found the bolometric luminosity, $L_{\rm bol} \sim$ 2–3 $\times$ 10^{44} erg s^{-1}, which is lower than that obtained during our observation. Our joint UV/X-ray spectral modeling suggests that the accretion disk emits like a standard disk down to $r_{\rm cor} \sim 39\, r_g$, while the inner disk is transformed into a warm corona. This is consistent with our UVIT/grating spectral

Table 4
Model Integrated Unabsorbed Continuum Fluxes of Different Emission Components Based on the OPTXAGNF/FAGNSED Models

Source	Mass ($10^8 M_\odot$)	Distance (Mpc)	Model	$F_{\rm disk}$ 0.001–0.01 keV (10^{-10})	$F_{\rm soft}$ 0.5–2 keV (10^{-11})	$F_{\rm hard}$ 2–10 keV (10^{-11})	$\frac{L_{\rm Bol}}{L_{\rm Edd}}$	$\frac{L_{0.001-0.1\,\rm keV}}{L_{\rm bol}(0.001-100\,\rm keV)}$
PG0804	5.4[a]	447.5	OPTXAGNF	1.85	0.1	1.0	0.54	0.63
			FAGNSED	0.88	0.2	1.0	0.20	0.14
NGC 7469	0.1[b]	68.7	OPTXAGNF	1.39	13.9	3.8	0.72	0.32
			FAGNSED	1.17	17.2	3.9	0.72	0.07
SWIFT 1921	0.39[c]	158	OPTXAGNF	0.29	1.4	5.2	0.56	0.03
			FAGNSED	1.01	1.4	5.2	0.98	0.06
SWIFT 1835	10[d]	233.8	OPTXAGNF	0.5	0.2	2.7	0.01	0.2
			FAGNSED	0.7	0.2	2.7	0.01	0.2

Notes. All the fluxes are in units of erg cm^{-2} s^{-1}. Bolometric luminosities are calculated from the model-integrated fluxes.
[a] Blackhole mass taken from M. C. Bentz & S. Katz (2015).
[b] Blackhole mass taken from B. M. Peterson et al. (2004).
[c] Blackhole mass taken from J.-M. Wang & E.-P. Zhang (2007).
[d] Blackhole mass taken from D. Marchesini et al. (2004).

analysis in Paper I, where we found the standard accretion disk to be truncated at 35–115 r_g.

M. Mehdipour et al. (2018) modeled the broadband data acquired with SWIFT-UVOT, Hubble Space Telescope, and Chandra using disk blackbody, warm Comptonization, hard X-ray power law, and a reflection model in two epochs, 2002 and 2015. They found that both the UV/optical and soft X-ray luminosity followed a similar trend, while the hard X-ray luminosity appears to be uncorrelated in 2002 and 2015 (see Table 5). Based on these two epochs of observations, they concluded the soft X-ray excess may favor warm Comptonization. Adding to that, with our AstroSat observation, we found the trend to be consistent with that found by M. Mehdipour et al. (2018). Apparently, in these three epochs, the UV and soft X-ray show a similar trend, favoring the warm Comptonization model as the origin of soft excess.

4.3. SWIFT J1921.1−5842

The UVIT/grating analysis with the DISKBB model predicted high inner disk temperature ($kT_{\rm in} > 23$ eV), and the OPTXAGNF model resulted in a poor quality fit (χ^2/dof = 492/321) for a maximally rotating black hole (see Paper I). These results based on DISKBB and OPTXAGNF may indicate that the UVIT/grating energy band in SWIFT1921 is significantly contributed by high-energy thermal Comptonized disk photons rather than standard or color-corrected accretion disk emission. The UV/X-ray spectral analysis resulted in a large $r_{\rm cor} \sim 95\, r_g$. Apparently, a large fraction of the BBB is contributed by the Comptonized photons. A similar scenario is observed in Fairall 9 by S. Hagen & C. Done (2023).

In Table 6, $F_{\rm UV}$ in 2007 represents the Galactic reddening–corrected average UVW2 filter flux (3.3×10^{-14}erg cm^{-2} s^{-1} Å^{-1}) for the three XMM-Newton observations during 2007 October. The total flux in the 50 nm wide band (5.2–6.6 eV) will be 1.6×10^{-11} erg cm^{-2} s^{-1}. It can be seen from Figure 6 that the flux in all three components (UV, soft X-ray, and hard X-ray) during our observation has increased by a factor of ∼2–4 (see also Table 6). The Eddington ratio in our observation is higher ($L_{\rm bol}/L_{\rm Edd} \sim$ 0.6–1) than that inferred ($L_{\rm bol}/L_{\rm Edd} \sim$ 0.12–0.42) from the broadband X-ray spectral modeling by R. Ghosh & S. Laha (2020). Additionally, they found the soft X-ray and the Galactic extinction–corrected UV flux measured at 2120 Å (UVW2 filter) to be uncorrelated.

The large inner disk radius obtained in our UV/X-ray spectral fitting may favor the warm Comptonization as the soft excess emission. However, based on the broadband X-ray modeling with XMM-Newton-NuSTAR, R. Ghosh & S. Laha (2020) concluded that both the warm Comptonization and the blurred reflection model describe the soft excess well. P. Gondoin et al. (2003) found a spectral slope of $\Gamma \sim 1.78$ and the 2–10 keV absorbed flux $\sim 2.65 \times 10^{-11}$erg cm^{-2} s^{-1} using the XMM-Newton observation performed in 2001. We

Table 5
NGC 7469: Intrinsic Luminosities (in Units of 10^{43} erg s^{-1}) of Different Emission Components in NGC 7469

Year	$L_{\rm disk}$ (1000–7000 Å)	$L_{\rm soft}$ (0.2–2 keV)	$L_{\rm hard}$ (2–10 keV)
2002	6.3	1	3.5
2015	5.5	0.8	4.7
2017	8.3	21.5	2.0

Note. The luminosities in 2002 and 2015 are quoted from XMM-Newton observations (M. Mehdipour et al. 2018), while those in 2017 are derived in this work.

Table 6
SWIFT1921: The Fluxes (in Units of 10^{-11} erg cm^{-2} s^{-1}) in 2007 Are Adopted from R. Ghosh & S. Laha (2020) and Those in 2018 Are from This Work

Observation Year	$F_{\rm UV}$ (1870–2370 Å)	$F_{\rm soft}$ (0.2–2 keV)	$F_{\rm hard}$ (2–10 keV)
2007	1.60	2.22	2.23
2018	2.97	7.95	5.15

Note. The first column lists the Galactic extinction–corrected flux in the XMM-Newton/OM-UVW2 filter (2007; adopted from R. Ghosh & S. Laha 2020). We calculated the $F_{\rm UV}$ (2018) by integrating the extinction-corrected best-fit model flux in the UVW2 wave band. The last two columns represent the unabsorbed continuum fluxes of the soft and hard X-ray emissions in SWIFT1921.

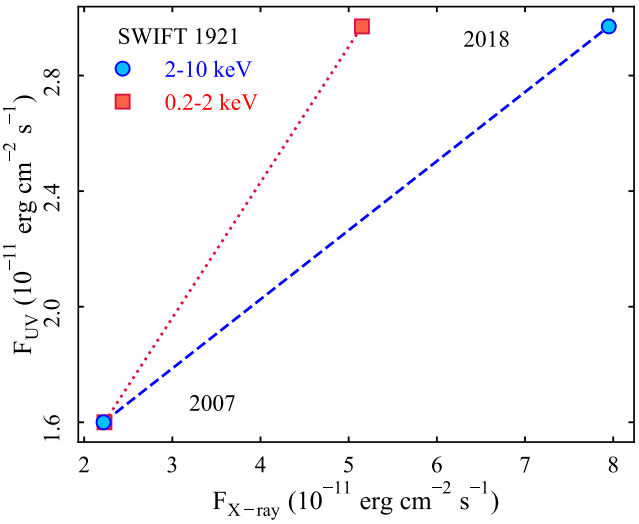

Figure 6. Unabsorbed flux variation in 2007 (R. Ghosh & S. Laha 2020) and 2018 (AstroSat). The F_{UV} is the model-integrated Galactic absorption–corrected flux in the wavelength range 1870–2370 Å.

found a steeper $\Gamma \sim 2$ and higher 2–10 keV absorbed flux $\sim 3.3 \times 10^{-11}$ erg cm^{-2} s^{-1}, which may indicate that the thermal (hot) Comptonization is responsible for the UV and hard X-ray spectral variability in this source.

4.4. SWIFT J1835.0+3240

The r_{cor} inferred from our broadband spectral modeling is consistent with that derived using the UVIT/grating spectral analysis in Paper I. We obtained the 2–10 keV flux, $\sim 2.8 \times 10^{-11}$ erg cm^{-2} s^{-1}, and the X-ray power-law slope, $\Gamma = 1.56^{+0.07}_{-0.09}$. Utilizing the data acquired with XMM-Newton/OM (Optical/UV Monitor) filters (U, UVW2, and UVM2), EPIC-pn, and NuSTAR in 2016, F. Ursini et al. (2018) modeled their UV–X-ray spectra with Fe II and Balmer continuum (small blue bump in UV), two thermal Comptonization models (warm and hot), one warm absorber, and two emission lines (in X-ray). They found the 2–10 keV flux varied in the range 3.4–4.2 $\times 10^{-11}$ erg cm^{-2} s^{-1} (Table 7), while the Γ_h remained fairly constant at $\sim$1.8. By modeling our UV/X-ray spectra with two thermal Comptonization models and one warm absorber component, we found a lower ($kT_{disk} < 1.45$ eV) disk temperature than that obtained by F. Ursini et al. (2018) ($\sim$3.4 eV). In addition, we found the accretion rate ($L_{Bol}/L_{Edd} \sim 0.01$) to be 50%–60% lower than that observed during 2016 by F. Ursini et al. (2018). The low accretion rate coupled with a harder photon index compared to the previous observation may indicate a transition from a bright/soft state to a dim/hard state. A similar spectral hardening has been observed by D. Ballantyne et al. (2014). Based on two epochs of NuSTAR observations in 2007 and 2008, they observed a higher coronal temperature and harder Γ in the low X-ray flux state (2–10 keV) compared to those in the high flux state. They concluded that the observed coronal heating is the consequence of the Comptonization of disk seed photons, typically observed in many Seyfert galaxies (G. Dewangan et al. 2002; A. A. Zdziarski et al. 2003; P. Tripathi et al. 2021).

We found the 0.3–2 keV flux and the electron temperature of the warm plasma ($kT_w \sim 0.16$ keV) lower (see Table 8) than those obtained by F. Ursini et al. (2018; $kT_w \sim 0.5$ keV).

Table 7
SWIFT1835: All the Values Are in Units of erg cm^{-2} s^{-1}

Observation Year	$F_{5.2-6.6\,eV}$ (10^{-12})	$F_{0.3-2\,keV}$ (10^{-12})	$F_{2-10\,keV}$ (10^{-11})
2016(O1)	6.1	8	3.4
2016(O5)	7.5	18	4.2
2018	4.9	5.7	2.8

Note. The first two rows show the highest (O5) and the lowest fluxes (O1) observed by F. Ursini et al. (2018) in five epochs of observation during 2016 using the data acquired with XMM-Newton/NuSTAR. The model-integrated fluxes in the last row are obtained from the AstroSat observation.

Table 8
SWIFT1835: The Model Expression in XSPEC:
TBABS × XABS × REDDEN × (NTHCOMP^h + NTHCOMP^w + GAUSSIAN +GAUSSIAN+GAUSSIAN)

Γ_w	kT_w (keV)	kT_{disk} (eV)	Norm$_w$ (10^{-4})	Γ_h	Norm$_h$ (10^{-3})
$2.2^{+0.2}_{-0.2}$	$0.16^{+0.07}_{-0.09}$	<1.45	$7.2^{+6.7}_{-4.1}$	$1.56^{+0.07}_{-0.09}$	$5.3^{+0.4}_{-0.6}$

Therefore, the plasma temperature in the warm corona has reduced with the reduction in overall flux in the UV to hard X-ray band (see Table 7), indicating this to be associated with the change in the accretion rate.

5. Conclusions

We present the UV–X-ray broadband spectral analysis of four type 1 AGN: PG0804, NGC 7469, SWIFT1921, and SWIFT1835 utilizing AstroSat observations. We found the soft excess to be consistent with the warm Comptonization in these sources. The main results of our SED modeling are described below:

1. PG0804 shows little to no flux variation in the emission components compared to the previous observations in 2010 with XMM-Newton (P. O. Petrucci et al. 2018). Our UV/X-ray data are better described by a standard outer disk and inner warm and hot corona. We obtained the spin parameter of $0.76^{+0.08}_{-0.20}$ (1σ error) with the FAGNSED.
2. We found that NGC 7469 favors the warm Comptonization scenario for the origin of soft excess. This source appears to exhibit low to moderate black hole spin ($a^\star < 0.67$).
3. For SWIFT 1921, we found that the fluxes in all three components, UV, soft X-ray excess, and X-ray power law, are twice higher than R. Ghosh & S. Laha (2020) during our observation. The standard disk appears truncated at a large radius of $95\,r_g$. The hard X-ray spectral slope is consistent with R. Ghosh & S. Laha (2020).
4. In the case of SWIFT 1835, both the UV/optical and X-ray fluxes decreased during our observation compared to the XMM-Newton observations by F. Ursini et al. (2018). Their X-ray power-law photon index ($\Gamma \sim 1.78$) and Eddington ratio ($0.02 - 0.03$) differ from those during our observation ($\Gamma \sim 1.56$, $L_{Bol}/L_{Edd} \sim 0.01$). The hardening of Γ with the reduction in the disk temperature and accretion rate may indicate a state transition from a high/soft to a low/hard state in this source.

Acknowledgments

This publication uses data from Indian Space Science Data Centre (ISSDC) of the AstroSat mission of the Indian Space Research Organisation (ISRO) and XMM-Newton. We acknowledge the SXT POC at TIFR (Mumbai) and UVIT POC at IIA (Bangalore) for providing the necessary software tools for data processing. The UVIT data were processed by CCDLAB pipeline (J. E. Postma & D. Leahy 2017). This research has used the Python and Julia packages. This research has used the SIMBAD/NED database. S.K. acknowledges the University grant Commission (UGC), Government of India, for financial support. K. P. Singh thanks the Indian National Science Academy for support under the INSA Senior Scientist Programme. L.M. acknowledges support from her CITA National Fellowship (reference #DIS-2022-568580) administered by the University of Toronto.

Facility: AstroSat.

Software: XSPEC (K. Arnaud 1996), SAOImageDS 9 (W. A. Joye & E. Mandel 2003), Julia (J. Bezanson et al. 2017), Astropy (Astropy Collaboration et al. 2013, 2018).

ORCID iDs

G. C. Dewangan https://orcid.org/0000-0003-1589-2075
K. P. Singh https://orcid.org/0000-0001-6952-3887
P. Gandhi https://orcid.org/0000-0003-3105-2615
L. Mallick https://orcid.org/0000-0001-8624-9162
G. C. Stewart https://orcid.org/0000-0001-9097-6573
S. Bhattacharyya https://orcid.org/0000-0002-6351-5808
S. Chandra https://orcid.org/0000-0002-8776-1835

References

Antia, H., Yadav, J., Agrawal, P., et al. 2017, ApJS, 231, 10
Arnaud, K. 1996, ASPC, 101, 17
Arnaud, K. A., Branduardi-Raymont, G., Culhane, J. L., et al. 1985, MNRAS, 217, 105
Astropy Collaboration, Price-Whelan, A. M., Sipőcz, B. M., et al. 2018, AJ, 156, 123
Astropy Collaboration, Robitaille, T. P., Tollerud, E. J., et al. 2013, A&A, 558, A33
Ballantyne, D., Bollenbacher, J., Brenneman, L., et al. 2014, ApJ, 794, 62
Bentz, M. C., & Katz, S. 2015, PASP, 127, 67
Bezanson, J., Edelman, A., Karpinski, S., & Shah, V. B. 2017, Soc. Ind. Appl. Math. Rev., 59, 65
Boissay, R., Paltani, S., Ponti, G., et al. 2014, A&A, 567, A44
Chen, S.-J., Wang, J.-X., Kang, J.-L., et al. 2025, ApJ, 980, 23
Dewangan, G., Boller, T., Singh, K., & Leighly, K. 2002, A&A, 390, 65
Dewangan, G. C. 2021, JApA, 42, 49
Dewangan, G. C., Griffiths, R. E., Dasgupta, S., & Rao, A. R. 2007, ApJ, 671, 1284
Done, C., Davis, S., Jin, C., Blaes, O., & Ward, M. 2012, MNRAS, 420, 1848
García, J., Dauser, T., Lohfink, A., et al. 2014, ApJ, 782, 76
García, J. A., Fabian, A. C., Kallman, T. R., et al. 2016, MNRAS, 462, 751
George, I., & Fabian, A. 1991, MNRAS, 249, 352
Ghosh, R., & Laha, S. 2020, MNRAS, 497, 4213
Gierliński, M., & Done, C. 2004, MNRAS, 349, L7
Gondoin, P., Orr, A., & Lumb, D. 2003, A&A, 398, 967
Grafton-Waters, S., Branduardi-Raymont, G., Mehdipour, M., et al. 2020, A&A, 633, A62
Hagen, S., & Done, C. 2023, MNRAS, 525, 3455
Joye, W. A., & Mandel, E. 2003, ASPC, 295, 489
Koratkar, A., & Blaes, O. 1999, PASP, 111, 1
Kubota, A., & Done, C. 2018, MNRAS, 480, 1247
Kumar, S., Dewangan, G., Singh, K., et al. 2023, ApJ, 950, 90
Mallick, L., Alston, W. N., Parker, M. L., et al. 2018, MNRAS, 479, 615
Mallick, L., Dewangan, G. C., McHardy, I. M., & Pahari, M. 2017, MNRAS, 472, 174
Mallick, L., Fabian, A., García, J., et al. 2022, MNRAS, 513, 4361
Marchesini, D., Celotti, A., & Ferrarese, L. 2004, MNRAS, 351, 733
Mehdipour, M., Kaastra, J., Costantini, E., et al. 2018, A&A, 615, A72
Middei, R., Petrucci, P.-O., Bianchi, S., et al. 2020, A&A, 640, A99
Noda, H., Makishima, K., Yamada, S., et al. 2011, PASJ, 63, S925
Pal, M., Dewangan, G. C., Misra, R., & Pawar, P. K. 2016, MNRAS, 457, 875
Peretz, U., Behar, E., Kriss, G., et al. 2018, A&A, 609, A35
Peterson, B. M., Ferrarese, L., Gilbert, K. M., et al. 2004, ApJ, 613, 682
Petrucci, P. O., Maraschi, L., Haardt, F., & Nandra, K. 2004, A&A, 413, 477
Petrucci, P. O., Ursini, F., De Rosa, A., et al. 2018, A&A, 611, A59
Postma, J. E., & Leahy, D. 2017, PASP, 129, 115002
Shakura, N. I., & Sunyaev, R. A. 1973, A&A, 24, 337
Singh, K., Garmire, G., & Nousek, J. 1985, ApJ, 297, 633
Singh, K., Stewart, G., Westergaard, N., et al. 2017, JApA, 38, 29
Singh, K. P., Stewart, G. C., Chandra, S., et al. 2016, SPIE, 9905, 99051E
Singh, K. P., Tandon, S., Agrawal, P., et al. 2014, SPIE, 9144, 91441S
Tandon, S., Postma, J., Joseph, P., et al. 2020, AJ, 159, 158
Tandon, S., Subramaniam, A., Girish, V., et al. 2017, AJ, 154, 128
Tripathi, P., Dewangan, G. C., Papadakis, I., & Singh, K. 2021, ApJ, 915, 25
Tripathi, S., Waddell, S., Gallo, L., Welsh, W., & Chiang, C. 2019, MNRAS, 488, 4831
Ursini, F., Petrucci, P., Matt, G., et al. 2018, MNRAS, 478, 2663
Vadawale, S. V., Rao, A. R., Bhattacharya, D., et al. 2016, SPIE, 9905, 409
Waddell, S., Gallo, L., Gonzalez, A., Tripathi, S., & Zoghbi, A. 2019, MNRAS, 489, 5398
Wang, J.-M., & Zhang, E.-P. 2007, ApJ, 660, 1072
Yadav, J., Agrawal, P., Antia, H., et al. 2016, SPIE, 9905, 99051D
Zdziarski, A. A., Lubiński, P., Gilfanov, M., & Revnivtsev, M. 2003, MNRAS, 342, 355